OPTICS

Deep tissue optical focusing and optogenetic modulation with time-reversed ultrasonically encoded light

Haowen Ruan,[1]* Joshua Brake,[1]* J. Elliott Robinson,[2] Yan Liu,[1] Mooseok Jang,[1†] Cheng Xiao,[2‡] Chunyi Zhou,[2‡] Viviana Gradinaru,[2] Changhuei Yang[1§]

Noninvasive light focusing deep inside living biological tissue has long been a goal in biomedical optics. However, the optical scattering of biological tissue prevents conventional optical systems from tightly focusing visible light beyond several hundred micrometers. The recently developed wavefront shaping technique time-reversed ultrasonically encoded (TRUE) focusing enables noninvasive light delivery to targeted locations beyond the optical diffusion limit. However, until now, TRUE focusing has only been demonstrated inside nonliving tissue samples. We present the first example of TRUE focusing in 2-mm-thick living brain tissue and demonstrate its application for optogenetic modulation of neural activity in 800-μm-thick acute mouse brain slices at a wavelength of 532 nm. We found that TRUE focusing enabled precise control of neuron firing and increased the spatial resolution of neuronal excitation fourfold when compared to conventional lens focusing. This work is an important step in the application of TRUE focusing for practical biomedical uses.

INTRODUCTION

Optical methods are widely used across biomedical research, as well as for the diagnosis and treatment of disease, yet the ability to monitor and modulate biological processes at depth is conventionally limited by light scattering caused by the heterogeneous optical properties of biological samples. For example, a 532-nm photon experiences an average of nearly 40 scattering events as it travels through 1 mm of mouse brain tissue (scattering mean free path $l \approx 26$ μm) (1, 2), which exemplifies why the formation of an optical focus in typical tissue samples is often limited to depths of a few hundred micrometers. To focus light deeper inside the tissue, wavefront shaping or wavefront engineering methods (3–10) have been developed that counteract the effects of optical scattering by modulating the incident light field so that the scattered light controllably interferes at locations of interest to form tight foci. This class of methods provides an advantage over techniques that discard scattered light as noise, such as confocal microscopy, because the probability of photons being unscattered (that is, ballistic in nature) decays exponentially with increasing depth. The incorporation of scattered photons enables light focusing beyond the optical diffusion limit where the propagation directions of the photons become random (11). Furthermore, because wavefront shaping techniques actively control scattered light, they offer direct optical modulation, an advantage over other optical imaging techniques such as photoacoustic tomography (11) and diffuse optical tomography (12), which enable deep tissue imaging, but cannot focus light to a particular location for improved light delivery.

The ability to manipulate scattered photons to create a light focus at depth with wavefront shaping is due to the elastic, deterministic nature of optical scattering, which scrambles but does not eliminate the information contained within a light field (13). Thus, if one could discern the positions and scattering profile of the scatterers within the medium, it would be possible to tailor an incident wavefront to optimally couple light to any point in the tissue. This process can be simplified by mapping the optical phase and/or amplitude relationship between the input plane outside the sample and the targeted plane inside, which can be accomplished through feedback-based approaches (3, 8, 14, 15), transmission matrix measurement (9, 10, 16–19), or optical time reversal (optical phase conjugation) (13, 20–24). Among these, optical phase conjugation is well suited for optical focusing in living tissue applications because it allows for measurement of the phase relationship between the target focus and the wavefront solution on the input plane in parallel, thus producing the fastest focusing speeds (25–30). This feature helps to overcome challenges posed by living tissue dynamics, which require that the wavefront shaping system obtain and playback the wavefront solution before the scatterers' configuration in the tissue changes (25–27, 30). When used with a guidestar (5), a method for tagging photons that traverse a desired location within the biological sample, the optical phase conjugation approach can create a phase conjugate wavefront that forms a focus at the guidestar location.

Several guidestar mechanisms have been developed that enable the generation of appropriate input wavefronts. These include fluorescent (31, 32), nonlinear optical (22, 33–36), kinetic (37, 38), photoacoustic (39–42), ultrasonic (43–46), magnetic (47), and microbubble (48) encoded mechanisms. Of these, ultrasound offers the advantage of being noninvasive, freely addressable within the volume of interest, and compatible with optical phase conjugation because it generates coherent tagged light. Time-reversed ultrasonically encoded (TRUE) focusing is a wavefront shaping technique that combines optical phase conjugation with the ultrasound guidestar to enable light focusing at depths beyond the optical diffusion limit with ultrasonic resolution (~30 μm) (44–46).

The application of TRUE focusing to living systems would be beneficial to many fields of study, including neurobiological research, in which visible light is routinely used for both monitoring activity with

[1]Department of Electrical Engineering, California Institute of Technology, 1200 East California Boulevard, Pasadena, CA 91125, USA. [2]Division of Biology and Biological Engineering, California Institute of Technology, Pasadena, CA 91125, USA.
*These authors contributed equally to this work.
†Present address: Department of Physics, Korea University, 145 Anam-ro, Seongbuk-gu, Seoul 02841, South Korea.
‡Present address: School of Anesthesiology, Xuzhou Medical University, Xuzhou, Jiangsu 221004, China.
§Corresponding author. Email: chyang@caltech.edu

genetically encoded neural activity indicators (49, 50) and controlling activity via optogenetic actuators (51). Although neurophotonic techniques that use multiphoton excitation (52–57) and adaptive optics (33, 34, 36) have extended the depths of optical access in vivo, focusing light noninvasively in the multiple scattering regime in living brain tissue remains largely unexplored. Because of the strongly scattering nature of brain tissue, light delivery during optogenetic manipulation still requires the use of invasive, implanted optical fibers to reach targets in deep brain regions (58). Because TRUE focusing allows for an optical focus to be formed noninvasively with the ability to freely move the focus within the tissue to target different regions of interest, it is particularly well suited for optogenetic modulation. Here, we describe the design and application of an integrated TRUE focusing and patch clamp electrophysiology system for simultaneous optogenetic stimulation and neural activity monitoring within living brain tissue ex vivo. We first demonstrate light focusing through up to 2-mm-thick living brain tissue using diffuse photons with a wavelength of 532 nm. Then, by performing patch clamp recordings in 800-μm-thick acute brain slices and using optogenetically evoked photocurrents as a readout, we demonstrate that TRUE focusing increases the spatial resolution of neuronal excitation by four times compared to that of conventional focusing at a wavelength of 532 nm. This result represents the first demonstration of TRUE focusing in living brain tissue and is an important step in the translation of wavefront shaping methods into practical optical tools for in vivo applications, including optogenetics.

RESULTS

System design and operating principles

To achieve TRUE focusing in living brain tissue ex vivo, we designed and implemented a digital optical phase conjugation (DOPC) system (21, 22) for TRUE focusing (figs. S1 and S2) that included an integrated patch clamp electrophysiology head stage and amplifier for neurophysiological measurements, as well as a removable differential interference contrast (DIC) microscope for neuron visualization while whole-cell recordings were being obtained (Fig. 1). A customized sample chamber was designed that allowed acute brain slices to rest horizontally while constantly perfused with carbogenated artificial cerebral spinal fluid (aCSF). Because this setup limited the orientations of the TRUE focusing light path and the ultrasound transducer to oblique angles, we illuminated the slice at a 45° angle with the ultrasound transducer positioned orthogonal to the TRUE light beam to maximize the modulation efficiency. To allow for the use of high numerical aperture (NA) lenses (for the DIC microscope objective, collection lens, and ultrasound transducer) with relatively short working distances to be operated within the limited available space, the observation objective, collection lens with lens tube, and ultrasound transducer were placed on computer-controlled motorized stages so they could be precisely translated in and out of the bath. To prevent fluctuations of the perfusion fluid surface from influencing the wavefront measurement, we attached a glass window to the lens tube and immersed it in the aCSF solution. This normally incident design also avoids unnecessary refraction at the aCSF-air interface. Similarly, the bottom of the chamber was also designed with a 45° chamber-air interface, which minimizes the effects of refraction and helps with optical alignment.

The creation of a TRUE focus involved sequential wavefront recording (Fig. 2A1) and playback (Fig. 2A2) steps. In the recording step, a high-frequency (50 MHz) ultrasound field was focused to the location of interest while a probe light beam generated by a pulsed 532-nm

laser illuminated the sample. Because of the acousto-optic effect, the frequency of a portion of the light passing through the ultrasound focus was shifted by the ultrasound frequency. The field of the scattered, ultrasound-tagged light was measured by the camera of the DOPC system using interferometry (59). Then, in the playback step, the phase conjugate version of the phase map of the ultrasound-tagged light was displayed on the spatial light modulator (SLM) of the DOPC system and used to create the playback light field. Following the principle of time reversal, this playback beam scattered in a time-reversed fashion and formed an optical focus at the location of the ultrasound focus. Our TRUE focusing system described here relied on a digital wavefront recording and playback engine (21, 22), which, compared with analog TRUE focusing systems (44), allowed for measured wavefronts to be played back at a light intensity far greater than that of the measured wave (45).

The average intensity of the TRUE focus compared to the background intensity for phase-only modulation of the wavefront is given by Eq. 1 (32)

$$\eta_{\text{phase-only}} = \frac{\pi}{4} \times \frac{(N-1)}{M} + 1 \tag{1}$$

where N is the number of optical modes controlled by the SLM and M is the number of optical modes (speckle grains) within the ultrasound
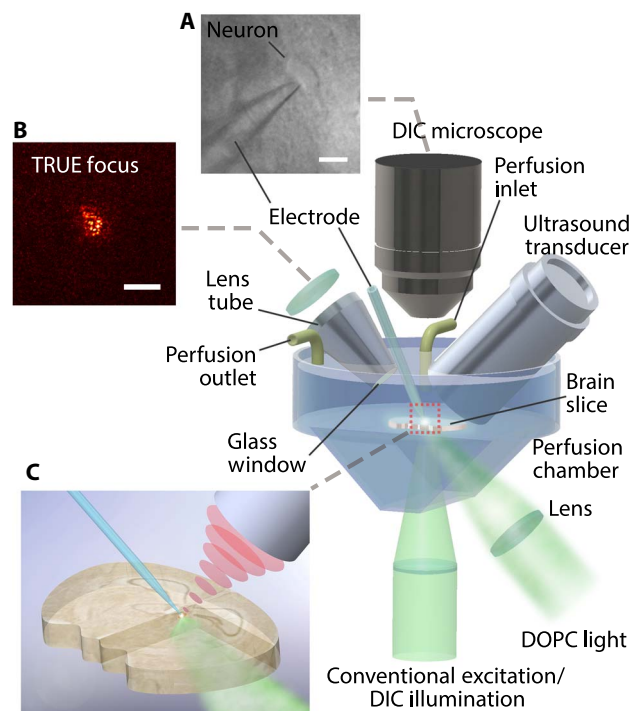

Fig. 1. Custom TRUE focusing and electrophysiological recording system. The custom TRUE focusing system combined a DOPC system with a patch clamp electrophysiology amplifier and headstage. Acute brain slices were held in a custom perfusion chamber that contained warmed, carbogenated aCSF. The TRUE light beam illuminated the tissue at an oblique 45° angle, and the borosilicate patch pipette electrode was used for neurophysiological measurements. (**A**) A DIC microscope was included for neuron visualization during patch clamping. (**B**) The TRUE focusing system allowed light to be sharply focused through the brain slice. (**C**) A close-up image of the TRUE focus on a patched neuron. Scale bars, 20 μm in (A) and 50 μm in (B).
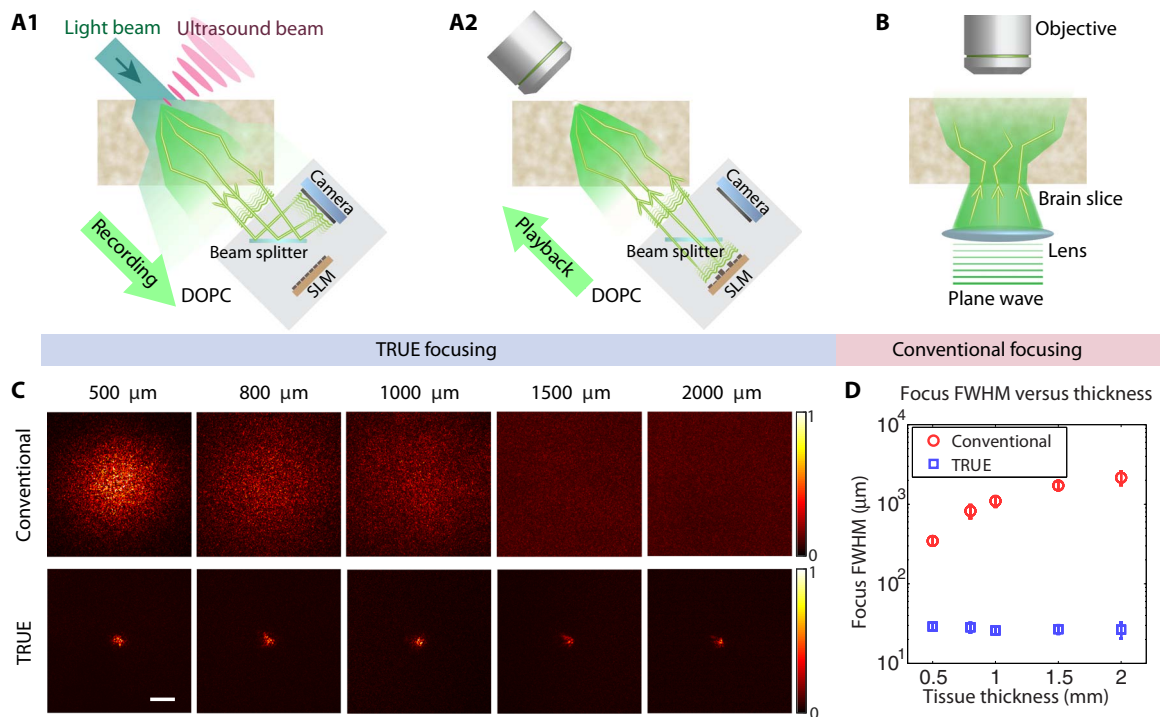
Fig. 2. A comparison of TRUE focusing and conventional focusing. (**A**) The recording (A1) and playback (A2) procedures used to focus light through the slice onto its top surface with TRUE focusing. (**B**) Diagram of the experimental setup for measuring the light intensity distribution of the focus on the top surface of the brain slice achieved using a conventional lens illuminating the brain slice from below. A tube lens and a camera used together with the objective are not shown. (**C**) Images of the conventional and TRUE focus profile through living brain tissue slices (500, 800, 1000, 1500, and 2000 μm thick). (**D**) Full width at half maximum (FWHM) focal spot sizes for the conventional and TRUE foci as a function of tissue thickness. Error bars represent the SD of five measurements taken at different locations. Scale bar, 100 μm.

focus. The size of the TRUE focus along the ultrasound beam lateral direction is dictated by the diffraction-limited focused ultrasound beam diameter, and the size along the ultrasound beam axial direction is determined by the ultrasound and laser pulse widths. To enhance the spatial resolution and contrast of TRUE focusing, we used an iterative TRUE focusing scheme (60–62), where the intensity and resolution of the TRUE focus were iteratively enhanced by repeating the TRUE focusing procedure using a previously established TRUE focus. A random phase pattern was displayed on the SLM to initiate the iterative TRUE focusing process. Rather than using two DOPC systems as previously demonstrated (61), we designed and implemented the iterative TRUE focusing system in transmission mode using a single DOPC system (see Materials and Methods and figs. S1 and S2 for detailed descriptions).

A comparison between TRUE and conventional focusing in living brain slices

To test the performance of our system, we prepared acute brain slices (300 to 2000 μm) that contained the medial prefrontal cortex (mPFC) from C57Bl/6J mice using a vibrating microtome as previously described (63, 64). Then, we placed the slices in our optical setup and recorded the light intensity profile through the slices formed by our TRUE focusing system (Fig. 2, A1 and A2) and a conventional lens (Fig. 2B). As predicted, the conventional focusing lens failed to form a tight optical focus and demonstrated a light profile that broadened as the brain slice thickness was increased due to the strong scattering nature of the tissue (Fig. 2C, top row). While a visible envelope of the intensity profile was observed when light was conventionally focused through a 500-μm-thick slice, the lateral width of the focus profile was signif-

icantly increased from the diffraction-limited focus size of ~1 μm (the NA of the focusing lens was 0.25). The size of the conventional focus continued to broaden as slice thickness was increased, and no discernible focus envelope was visible within the 580 × 580–μm² field of view in the 1000-μm or thicker slices.

In contrast, TRUE focusing was able to maintain a lateral resolution defined by the size of the ultrasound focus, decoupling the size of the focus from the focusing depth (Fig. 2C, bottom row). Our system used a high-frequency ultrasound transducer with a 50-MHz nominal center frequency, a 6.35-mm aperture, and a 12.7-mm focal length. The theoretical beam diameter (–6 dB) for this configuration was ~80 μm, and the calibrated waveform duration (–6 dB) was 37.4 ns, corresponding to a pulse length of 55.3 μm. The region of ultrasound-modulated light along the axial direction of the ultrasound beam was also determined by the combination of the ultrasound pulse length and the laser pulse duration, which is 7 ns. Using the iterative TRUE focusing method enabled the TRUE focus to be tightened (60) to achieve a focus with an average FWHM spot size of 27.4 μm across tissue thicknesses from 500 to 2000 μm (see method S1 for calculation). In contrast, the FWHM of the conventional focus broadened from ~350 μm at a slice thickness of 500 μm to approximately 2100 μm at a thickness of 2000 μm (Fig. 2D). It should be noted that the effective thicknesses in the TRUE focusing case are larger than the physical thicknesses of the slices due to the 45° incident angle of the TRUE focusing beam. These results demonstrate the ability of TRUE focusing to overcome optical scattering to create high-resolution optical foci in living brain slices up to 2000 μm thick, which, unlike those formed by conventional focusing, do not significantly broaden with increased sample thickness.

Application of TRUE focusing for optogenetic manipulations

After demonstrating the ability of TRUE focusing to overcome optical scattering and produce light foci in thick acute brain slices, we next sought to demonstrate the advantage of TRUE for optogenetic manipulation compared with conventional focusing using a neurophysiological readout. Optogenetics, in which engineered light-gated ion channels or pumps are used to manipulate cellular activity with high spatial and temporal precision using visible light, has become relatively ubiquitous in basic neurobiological research due to its ability to convert differences in light intensity into graded electrophysiological signals (51). Although a wide range of optogenetic actuators are available for neural excitation or inhibition with diverse excitation spectra spanning the visible spectrum, we used the excitatory, red-shifted opsin bReaChES for our experiments because its excitation peak was well matched with our laser source (532 nm) (65). To prepare samples for testing, we performed stereotaxic injections of an adeno-associated viral vector carrying the bReaChES transgene (AAV-DJ-CaMKII-bReaChES-TS-YFP) into the mPFC of C57Bl/6J mice (Fig. 3A). After waiting 4 weeks for surgical recovery and transgene expression, we prepared acute brain slices for simultaneous electrophysiological recording and optical testing. Animal husbandry and all experimental procedures involving animal subjects were approved by the Institutional Animal Care and Use Committee (IACUC) and by the Office of Laboratory Animal Resources at the California Institute of Technology under IACUC protocol 1650. We characterized the performance of bReaChES in cortical slices by measuring the photocurrent response to a wide range of 532-nm light intensities delivered through the DIC objective in voltage clamp mode. Similar to its parent opsin ReaChR (66), bReaChES displayed a nonlinear increase in photocurrent response that saturated at an intensity of approximately 10 mW/mm^2 (Fig. 3B). During these experiments, the average maximum photocurrent across the 10 cells studied was 1047 pA.

To demonstrate the capability of TRUE focusing for neural modulation, whole-cell patch clamp recordings were obtained from layer II/III neurons just below the superficial surface of mPFC slices using borosilicate glass patch pipette electrodes visualized under DIC microscopy (Fig. 1 and fig. S1C). Although TRUE focusing through slices up to 2 mm thick was achieved, maximum slice thickness during our optogenetic experiments was limited to 800 μm, because neurons in thicker slices were difficult to visualize with DIC microscopy and were generally less healthy, which negatively affects recording and data quality. Because target neurons were located close to the surface of the brain slice for visualization, the DOPC playback beam illuminated from the bottom of the slice traversed almost the entire sample thickness, which is much larger than the optical diffusion limit of the acute mouse brain slice (~200 μm at 532 nm) (2). Moreover, because the incident angle was 45° (Fig. 3C), the effective thickness for TRUE focusing was even larger than the physical slice thickness. Once a whole-cell recording was successfully initiated, the DIC microscope objective was removed, and the lens tube and ultrasound transducer were lowered into the bath. To ensure colocalization of the ultrasound focus with the pipette tip, we used pulse-echo ultrasound to form an image of the glass pipette tip (fig. S3) and moved the ultrasound transducer to focus on the end of the tip where a target neuron was located. This approach allowed precise targeting of the TRUE focus to the recording neuron to maximize light delivery during optogenetic stimulation.

Next, we measured the photocurrent response that was elicited by the TRUE focus; as a control, we created a "no wavefront shaping" condition by shifting the wavefront solution on the SLM by 100 pixels in each lateral direction, which generally approximated the laser background intensity. In this case, the TRUE focus outperformed the no shaping condition, evoking a larger photocurrent due to enhanced light intensity at the focus (Fig. 3D, left). The photocurrent enhancement factor, defined as the ratio between the difference of the photocurrent with and without TRUE focusing and the photocurrent without TRUE focusing, was on average 30% ($n = 6$) in 800-μm-thick brain slices, which was similar in magnitude to the enhancement observed in 300- and 500-μm slices (fig. S4). To verify the effect of the ultrasound guidestar, we turned off the ultrasound and repeated the same procedure. In this case, because there was no guidestar for the system to focus to, no TRUE focus was formed, resulting in a smaller evoked photocurrent and no observed firing events (fig. S5). Because the presence of the ultrasound field could potentially alter neural activity, we verified in several neurons that focused ultrasound alone in the absence of light failed to evoke any observable current in voltage clamp or alter neuronal excitability in current clamp mode.

We next sought to evaluate the performance of our system by comparing the experimentally observed enhancement factor with the expected enhancement predicted by the technical specifications of our system and the observed TRUE focus size. The SLM used in the DOPC system had 2×10^6 pixels, which allows us to focus light through a highly scattering medium to a single optical mode with an experimental peak focus intensity to background ratio η of ~1×10^4. This experimental performance means the DOPC system could effectively control $N \sim 1 \times 10^4$ optical modes. On the basis of this performance, we were able to estimate the intensity enhancement at the ultrasound focus using Eq. 1. Because our system produced a TRUE focus with a FWHM
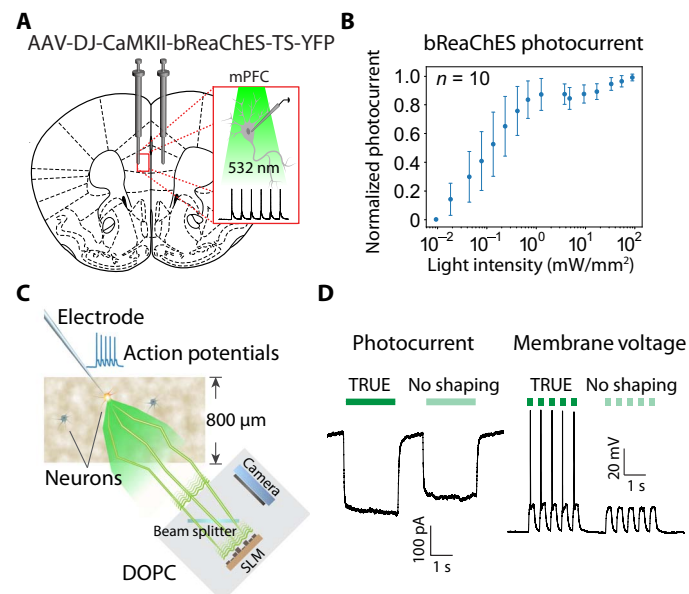

Fig. 3. Experiment design, opsin characterization, and demonstration of photocurrent and firing modulation via TRUE focusing. (**A**) An AAV vector was used to stereotaxically deliver the bReaChES transgene to the mPFC. (**B**) Characterization of normalized photocurrent response versus light intensity. The average maximum photocurrent across the 10 cells studied was 1047 pA. (**C**) Diagram illustrating the experimental scheme used to demonstrate the ability of TRUE focusing to elicit action potentials through 800-μm-thick living mouse brain tissue. (**D**) Representative traces demonstrating elicited photocurrent and membrane voltage changes achieved with and without TRUE focusing.

diameter of ~27 μm, the number of modes M inside the focus was ~1×10^4, which corresponded to a predicted intensity enhancement factor at the ultrasound focus of approximately 2. Because the photocurrent enhancement was not proportional to light intensity (Fig. 3B), we predicted that the photocurrent enhancement factor would be less than 1, which was consistent with our data. Despite the observed enhancement, the laser power could be adjusted so that the TRUE focus elicited time-locked cell firing, whereas the no shaping condition could not elicit action potentials (Fig. 3D, right).

Improved spatial resolution of optogenetic stimulation using TRUE focusing

After demonstrating that TRUE-focused light could optogenetically stimulate neurons at depths beyond the optical diffusion limit, we compared the spatial resolution of TRUE focusing with that of conventional lens focusing for optogenetic modulation. The ability for TRUE focusing to noninvasively enhance the light intensity in a spatially restricted manner is an important benefit compared to other conventional methods for delivering light into the brain, such as optical fibers or light-emitting diode (LED) implants, which do not allow for the targeted volume to be freely moved within the brain after implantation. To quantify the spatial resolution of TRUE focusing and conventional focusing, we raster-scanned the focus of each case laterally around a patch-clamped neuron and recorded the photocurrent magnitude at each scanning position (Fig. 4, A and B). In both cases, we scanned over a square grid of 9×9 points with a 50-μm step size in each dimension on the horizontal plane. For conventional focusing, the 780-nm wavelength DIC illumination LED was replaced with the 532-nm wavelength laser source delivered via a single-mode optical fiber whose tip was imaged to the plane of the targeted neuron to form a focus (fig. S1D). The position of the focus was calibrated using the observation microscope before placing the brain slice in the chamber, and the focus was raster-scanned on the horizontal plane during whole-cell recordings (fig. S1, C and D). The normalized photocurrent enhancement was calculated at each scanning position and used to construct interpolated two-dimensional (2D) scan maps (Fig. 4, C and D). Fitting the conventional lens scan map with a 2D Gaussian function yielded respective FWHMs of 393 and 536 μm in the x and y dimensions. In contrast, the FWHMs for the TRUE focusing scan were 99 and 71 μm in the x and y dimensions. Because of the scattering and diffusion of the conventional illumination, the spatial extent of the evoked photocurrent enhancement with conventional illumination was nearly four times broader than that obtained with TRUE focusing, thus confirming the utility of TRUE focusing for precise spatial focusing at depth beyond the optical diffusion limit.

DISCUSSION

Overcoming optical scattering to noninvasively extend the depth at which light can be tightly focused inside living biological samples in clinical and research settings is of great interest to practitioners and researchers alike. Here, we developed a TRUE focusing system that allowed us to focus light at depth in ex vivo brain tissue with a spatial resolution that significantly outperformed conventional lens focusing. By integrating a patch clamp electrophysiology headstage and amplifier into the TRUE focusing system, we were able to monitor neural activity during optogenetic stimulation with the TRUE focus. Using neurophysiological signals as a readout, we confirmed that TRUE focusing can be used to control neural activity in thick tissue samples in a spatially restricted

manner. Because optogenetic manipulations currently require the surgical implantation of invasive optical fibers for light delivery below the most superficial brain regions (58), we believe that our findings using TRUE focusing will inform future efforts to develop this technology for noninvasive optogenetic stimulation and/or fluorescent imaging in vivo with the spatial resolution required for precise targeting of individual neurons or neuron ensembles.

Multiphoton microscopy is capable of obtaining clear images at depths of 800 μm and is promising for neuromodulation at that depth. However, the fundamental working depth of this technique is limited by the number of unscattered or weakly scattered photons, which decreases exponentially with depth. In contrast, the TRUE focusing technique is able to focus light beyond the ballistic photon regime. The addressable depth of the TRUE focusing technique demonstrated in this set of optogenetic experiments was limited by the penetration depth of the DIC microscope illumination necessary to visualize neurons during the initiation of patch clamp recordings, as well as the viability of the neurons in thick tissue. Although fluorescent activity indicators, such as the GCaMP family of proteins (67), would provide a viable activity readout in thicker tissue samples, these tools were not practical for use here given that the excitation wavelength for calcium indicators is likely to simultaneously excite neurons with opsins that match the operating wavelength of the TRUE focusing system (532 nm). In the future, this problem could be solved by decoupling the wavelength for TRUE focusing and optogenetic excitation from that for calcium indicator excitation. It would also be valuable to explore the maximum penetration depth of TRUE focusing for optogenetics, even if it would require minimally invasive methods in vivo such as optical fiber insertion for signal readout.
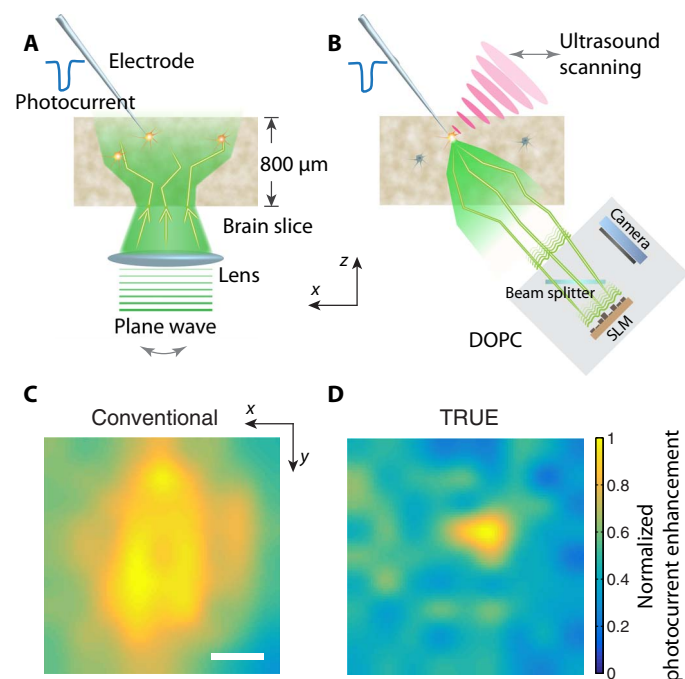

Fig. 4. Spatial resolution of optogenetic stimulation achieved by conventional versus TRUE focusing. Experimental configuration for photocurrent scan map generation using conventional focusing (**A**) and TRUE focusing (**B**). The normalized photocurrent enhancement as a function of lateral focal scanning position for conventional (**C**) and TRUE focusing (**D**). Scale bar, 100 μm.

Unlike in ex vivo tissue preparations where cell viability is a limiting factor for tissue thickness, the focusing depth during in vivo applications is limited by the guidestar efficiency. As we focus deeper into tissue, fewer photons from the guidestar can be measured, not only because the detected portion of light from the guidestar is reduced but also because of a decrease in the modulation efficiency due to ultrasound attenuation. Although the DOPC system works even when the measured phase map has less than a photon per degree of freedom (that is, SLM or camera pixel) (68), the presence of shot noise due to the much higher unmodulated light intensity will fundamentally limit the penetration depth (24, 69). Additional guidestar aids, such as microbubbles, can help improve the tagging efficiency significantly (48) but sacrifice the freely addressable and noninvasive nature of the ultrasound guidestar. In the future, it will be important to optimize the intensity of the measured ultrasound-modulated light to extend the penetration depth.

Another goal for future developments of TRUE focusing for optogenetic simulation is improved photocurrent enhancement. Using whole-cell recordings, we observed a photocurrent enhancement of approximately 30% compared to the no shaping condition, which was consistent with predicted values but will require improvement before TRUE focusing is feasible for widespread use in optogenetic applications. The avenues to improve the focusing contrast are based on the variables in Eq. 1. From this equation, we can see that to enhance the focusing contrast, we can either increase N, the number of controllable modes, or decrease M, the number of optical modes within the ultrasound focus. One way to reduce M is by reducing the size of the ultrasound focus by increasing the operating frequency and the NA of the ultrasound transducer. However, high-frequency ultrasound has a very limited penetration depth. Furthermore, because the goal is to enhance the light intensity delivered to the neuron soma, shrinking the size of the focus beyond the size of the cell will not necessarily lead to further improvements in photocurrent enhancement, although this strategy may allow for finer resolution targeting of neuronal subcompartments, such as individual dendrites or synaptic inputs. Another strategy is to increase the size of the optical modes by shifting to longer wavelengths, although opsins sensitive to infrared or near-infrared wavelengths will need to be further refined before they are practical for single photon in vivo applications (70, 71). A more feasible avenue to improve the TRUE focus contrast is to increase the number of controllable optical modes, N. This can be achieved by scaling up the number of SLM pixels, which will also benefit other general applications across the wavefront shaping field. For example, increasing the number of SLM pixels N by 10 times will result in a focus intensity–to–background ratio $\eta \approx 12$, which is sufficient for many practical applications.

To translate wavefront shaping into practical tools for in vivo applications, we also need to address the challenge of the optical decorrelation of living tissue. The dynamic nature of living tissue causes decorrelation of the optical wavefronts, so to effectively focus light inside living tissue, the system response time must be shorter than the decorrelation time of the tissue. For acute brain slices less than 2 mm in thickness, this decorrelation time is on the order of several seconds (72), which is longer than the current TRUE focusing speed (0.6 s; see fig. S2). However, the decorrelation time drops to the order of 1 ms for in vivo applications due to blood flow, cardiac motion, breathing, etc. (26, 73, 74). To increase the response speed of wavefront shaping systems, digital micromirror devices and ferroelectric liquid crystal–based SLMs have been used to achieve high-speed DOPC within 10 ms (25, 27), which is ultimately limited by the need to read out and transfer data to a computing device such as a personal computer or an embedded system to compute the appropriate wavefront solution.

We expect that solving these problems will require an integrated wavefront shaping system that combines the wavefront sensing and modulation devices into a single device (75). This design will allow for control over an increased number of optical modes in a scalable way without sacrificing the operation speed, because wavefront calculations can be performed in parallel on a per pixel basis, minimizing data transfer and computation time. The development of such an integrated wavefront sensing and modulation platform will increase the achievable enhancement factors. Simultaneously, it will remove many of the challenges that limit the widespread adoption of wavefront shaping techniques, such as the difficulty of designing and aligning the complex optical system (76), opening the door for more scientists to incorporate wavefront shaping into their optical technologies for biomedicine and beyond.

MATERIALS AND METHODS
Acute brain slice preparation
Stereotaxic injection of AAV-DJ-CaMKII-bReaChES-TS-YFP was used to deliver the opsin transgene into the mPFC in adult mice and allowed to express for 3 to 4 weeks before the experiments were conducted. On the day of each experiment, acute brain slices (300 to 2000 μm) that contained the infralimbic and prelimbic cortices were prepared with a vibrating microtome after euthanasia and transcardial perfusion with ice-cold cutting solution, as previously described (63, 64). Slices were recovered in 32°C, carbogenated aCSF for 1 hour before the start of each recording. Recordings were performed using a potassium gluconate internal solution in the presence of carbogenated aCSF that contained 3 mM kynurenic acid to block excitatory postsynaptic currents. Methods S2 and S3 describe sample preparation and recording conditions in greater detail.

TRUE focusing system design and integration of the patch clamp amplifier and head stage
The DOPC system consisted of three major modules (fig. S1, A and B): a light beam preparation module, a DOPC module, and the patch clamp electrophysiology amplifier/head stage. The light beam preparation module prepared three light beams for the DOPC system: a planar reference beam for wavefront recording (R), a sample or playback beam (S/PB) that illuminated the sample, and a quality assurance beam (QA) for daily system alignment. All three beams were spatially filtered, path-length–matched, and aligned to the horizontal polarization direction. For the S/PB beam, we used two laser sources, a nanosecond pulsed wave (PW) laser (532-nm wavelength, 7-ns pulse width, 40-kHz repetition rate, and 7-mm coherence length; Navigator, Spectra-Physics) for TRUE focusing and a continuous wave (CW) laser (532-nm wavelength; Millennia eV, Spectra-Physics) for optogenetic stimulation, which was modulated by an optical chopper. These two laser beams were selected by a beam selecting shutter (BSS1) and coupled to a pinhole-based spatial filter through a beam splitter (BS2). A 4f system (L1 and L2) was used to match the beam diameter of the PW laser to that of the CW laser beam so that they achieved optimum coupling efficiency through the pinhole. The frequency of the reference beam and QA beam was modulated by two acousto-optic modulators (AOM; AFM-502-A1, IntraAction).

The DOPC module used four beam splitters (BS4, BS5, BS8, and BS9) and two beam selecting shutters (BSS2 and BSS3) to route the

S/PB beam into two separated optical loops (loop A and loop B), which were used sequentially during iterative TRUE focusing operation. To initialize the iterative process, the SLM (PLUTO, HOLOEYE) displayed a random phase map to generate a disordered light field that mimicked the light inside the sample. The BSS2 and BSS3 were set to enable DOPC loop A, which directed the light to the sample from the top surface. The ultrasound-modulated light field was measured by the camera (Camera 1, pco.edge 5.5, PCO-TECH) of the DOPC system, and its conjugated phase map was displayed on the SLM. We then flipped BSS2 and BSS3 to enable DOPC loop B, which routed the shaped S/PB beam to the sample in the reversed direction (fig. S1B), resulting in an initial TRUE focus. The TRUE focus was modulated by the ultrasound again, and the ultrasound-modulated light was measured by the camera. Immediately, the SLM was updated and DOPC loop A was enabled again for the next iteration. By repeating the TRUE focusing process between these two DOPC loops nine times (nine SLM updates), we obtained an optimized wavefront solution for TRUE focusing. In this case, DOPC loop B is enabled and we switched the light source to the CW laser for neural modulation. An amplitude mask (ZB) was placed on the focal plane of lens L7 to block the zeroth order of the playback beam, which was not modulated by the SLM. The daily tuning procedure for the DOPC system can be found in method S4.

The electrophysiological recording setup had two operating modes, a neuron patching mode and a neuron stimulation mode (fig. S1, C and D). In the neuron patching mode (fig. S1C), the collection lens (L10) and its lens tube and the transducer were translated out of the chamber, allowing the objective (40×, LUMPlanFL/IR, Olympus) of a custom-built DIC microscope to be immersed into the solution for neuron visualization. We used a 780-nm LED (M780D2, Thorlabs) as the light source (LS1) to maximize the penetration depth. Once a whole-cell recording was initiated, we switched to the neuron stimulation mode (fig. S1D) by lifting the objective out of the perfusion chamber and translating the ultrasonic transducer (PI50, Olympus) and collection lens L10 and its lens tube down to the chamber. In this mode, we performed iterative TRUE focusing while photocurrents or transmembrane potentials were measured via the patch pipette electrode (PP). In the case of conventional focusing, we replaced the LED source with the 532-nm CW laser source delivered by a single-mode fiber (SF3) whose tip was imaged to the top surface of the sample. We raster-scanned the focus by scanning the tip of the single mode fiber SF3 on the focal plane of lens L17 while recording the transmembrane current at each scanning position. The electrophysiological signals were recorded by a computer-controlled patch clamp amplifier (EPC10 USB, HEKA) and filtered at 10 kHz.

Measurement of the phase map of the ultrasonically tagged light

A detailed signal flow diagram is shown in fig. S2. We used four-step phase-shifting holography (59) to measure the phase of the ultrasonically tagged light and shifted the phase of the reference beam by stepping the phase of the signal driving the AOM through 0, $\pi/2$, π, and $3\pi/2$. Four intensity maps (I_0, $I_{\pi/2}$, I_π, and $I_{3\pi/2}$) corresponding to each phase of the reference beam were recorded, and the phase map of the ultrasonically tagged light was calculated as $\phi = \mathrm{Arg}[(I_{\pi/2} - I_{3\pi/2}) + i(I_0 - I_\pi)]$, where $\mathrm{Arg}[\cdot]$ computes the principal value of the argument of a complex number. Because we used laser pulses with a pulse width smaller than 20 ns as the light source to ensure fine axial resolution of the TRUE focus, we needed to carefully design the parameters to eliminate the unwanted signal formed by the interference between the

reference beam (R) and the unmodulated sample beam (U), as well as the unwanted signal formed by the interference between the ultrasonically tagged light (T) and U, which would otherwise overwhelm the real signal formed by the interference between R and T. The formulation to design the timing for these three beams has been described previously (77), and a detailed signal diagram is illustrated in fig. S2.

SUPPLEMENTARY MATERIALS

Supplementary material for this article is available at http://advances.sciencemag.org/cgi/content/full/3/12/eaao5520/DC1

method S1. Calculation of the focal spot size of TRUE and conventional focusing.
method S2. Viral injection surgery.
method S3. Electrophysiological recordings.
method S4. Daily alignment procedure.
fig. S1. Setup.
fig. S2. Electrical signal flow diagram.
fig. S3. Ultrasound pulse-echo image of the tip of the glass pipette electrode.
fig. S4. Electrophysiological photocurrent traces from neurons in 500- and 300-µm-thick acute brain slices.
fig. S5. Electrophysiological photocurrent and membrane voltage traces comparing ultrasound on and off conditions.

REFERENCES AND NOTES

1. S. Schott, J. Bertolotti, J.-F. Léger, L. Bourdieu, S. Gigan, Characterization of the angular memory effect of scattered light in biological tissues. *Opt. Express* **23**, 13505–13516 (2015).
2. M. Mesradi, A. Genoux, V. Cuplov, D. Abi-Haidar, S. Jan, I. Buvat, F. Pain, Experimental and analytical comparative study of optical coefficient of fresh and frozen rat tissues. *J. Biomed. Opt.* **18**, 117010 (2013).
3. I. M. Vellekoop, A. P. Mosk, Focusing coherent light through opaque strongly scattering media. *Opt. Lett.* **32**, 2309–2311 (2007).
4. A. P. Mosk, A. Lagendijk, G. Lerosey, M. Fink, Controlling waves in space and time for imaging and focusing in complex media. *Nat. Photonics* **6**, 283–292 (2012).
5. R. Horstmeyer, H. Ruan, C. Yang, Guidestar-assisted wavefront-shaping methods for focusing light into biological tissue. *Nat. Photonics* **9**, 563–571 (2015).
6. H. Yu, J. Park, K. Lee, J. Yoon, K. Kim, S. Lee, Y. Park, Recent advances in wavefront shaping techniques for biomedical applications. *Curr. Appl. Phys.* **15**, 632–641 (2015).
7. S. Rotter, S. Gigan, Light fields in complex media: Mesoscopic scattering meets wave control. *Rev. Mod. Phys.* **89**, 015005 (2017).
8. I. M. Vellekoop, Feedback-based wavefront shaping. *Opt. Express* **23**, 12189–12206 (2015).
9. S. M. Popoff, G. Lerosey, M. Fink, A. C. Boccara, S. Gigan, Controlling light through optical disordered media: Transmission matrix approach. *New J. Phys.* **13**, 123021 (2011).
10. M. Kim, W. Choi, Y. Choi, C. Yoon, W. Choi, Transmission matrix of a scattering medium and its applications in biophotonics. *Opt. Express* **23**, 12648–12668 (2015).
11. L. V. Wang, S. Hu, Photoacoustic tomography: In vivo imaging from organelles to organs. *Science* **335**, 1458–1462 (2012).
12. D. A. Boas, D. H. Brooks, E. L. Miller, C. A. DiMarzio, M. Kilmer, R. J. Gaudette, Q. Zhang, Imaging the body with diffuse optical tomography. *IEEE Signal Process. Mag.* **18**, 57–75 (2001).
13. Z. Yaqoob, D. Psaltis, M. S. Feld, C. Yang, Optical phase conjugation for turbidity suppression in biological samples. *Nat. Photonics* **2**, 110–115 (2008).
14. J. Yoon, M. Lee, K. R. Lee, N. Kim, J. M. Kim, J. Park, H. Yu, C. Choi, W. D. Heo, Y. K. Park, Optogenetic control of cell signaling pathway through scattering skull using wavefront shaping. *Sci. Rep.* **5**, 13289 (2015).
15. R. Sarma, A. G. Yamilov, S. Petrenko, Y. Bromberg, H. Cao, Control of energy density inside a disordered medium by coupling to open or closed channels. *Phys. Rev. Lett.* **117**, 086803 (2016).
16. S. M. Popoff, G. Lerosey, R. Carminati, M. Fink, A. C. Boccara, S. Gigan, Measuring the transmission matrix in optics: An approach to the study and control of light propagation in disordered media. *Phys. Rev. Lett.* **104**, 100601 (2010).
17. Y. Choi, T. Daniel Yang, C. Fang-Yen, P. Kang, K. Jin Lee, R. R. Dasari, M. S. Feld, W. Choi, Overcoming the diffraction limit using multiple light scattering in a highly disordered medium. *Phys. Rev. Lett.* **107**, 023902 (2011).
18. H. Yu, T. R. Hillman, W. Choi, J. O. Lee, M. S. Feld, R. R. Dasari, Y. K. Park, Measuring large optical transmission matrices of disordered media. *Phys. Rev. Lett.* **111**, 153902 (2013).

19. D. B. Conkey, A. M. Caravaca-Aguirre, R. Piestun, High-speed scattering medium characterization with application to focusing light through turbid media. *Opt. Express* **20**, 1733–1740 (2012).

20. E. N. Leith, J. Upatnieks, Holographic imagery through diffusing media. *J. Opt. Soc. Am.* **56**, 523 (1966).

21. M. Cui, C. Yang, Implementation of a digital optical phase conjugation system and its application to study the robustness of turbidity suppression by phase conjugation. *Opt. Express* **18**, 3444–3455 (2010).

22. C.-L. Hsieh, Y. Pu, R. Grange, D. Psaltis, Digital phase conjugation of second harmonic radiation emitted by nanoparticles in turbid media. *Opt. Express* **18**, 12283–12290 (2010).

23. T. R. Hillman, T. Yamauchi, W. Choi, R. R. Dasari, M. S. Feld, Y. K. Park, Z. Yaqoob, Digital optical phase conjugation for delivering two-dimensional images through turbid media. *Sci. Rep.* **3**, 1909 (2013).

24. Y. Shen, Y. Liu, C. Ma, L. V. Wang, Focusing light through biological tissue and tissue-mimicking phantoms up to 9.6 cm in thickness with digital optical phase conjugation. *J. Biomed. Opt.* **21**, 085001 (2016).

25. D. Wang, E. Haojiang Zhou, J. Brake, H. Ruan, M. Jang, C. Yang, Focusing through dynamic tissue with millisecond digital optical phase conjugation. *Optica* **2**, 728–735 (2015).

26. Y. Liu, P. Lai, C. Ma, X. Xu, A. A. Grabar, L. V. Wang, Optical focusing deep inside dynamic scattering media with near-infrared time-reversed ultrasonically encoded (TRUE) light. *Nat. Commun.* **6**, 5904 (2015).

27. Y. Liu, C. Ma, Y. Shen, J. Shi, L. V. Wang, Focusing light inside dynamic scattering media with millisecond digital optical phase conjugation. *Optica* **4**, 280–288 (2017).

28. C. Ma, F. Zhou, Y. Liu, L. V. Wang, Single-exposure optical focusing inside scattering media using binarized time-reversed adapted perturbation. *Optica* **2**, 869–876 (2015).

29. Y. Liu, C. Ma, Y. Shen, L. V. Wang, Bit-efficient, sub-millisecond wavefront measurement using a lock-in camera for time-reversal based optical focusing inside scattering media. *Opt. Lett.* **41**, 1321–1324 (2016).

30. M. Jang, H. Ruan, I. M. Vellekoop, B. Judkewitz, E. Chung, C. Yang, Relation between speckle decorrelation and optical phase conjugation (OPC)-based turbidity suppression through dynamic scattering media: A study on in vivo mouse skin. *Biomed. Opt. Express* **6**, 72–85 (2015).

31. I. M. Vellekoop, M. Cui, C. Yang, Digital optical phase conjugation of fluorescence in turbid tissue. *Appl. Phys. Lett.* **101**, 081108 (2012).

32. I. M. Vellekoop, E. G. van Putten, A. Lagendijk, A. P. Mosk, Demixing light paths inside disordered metamaterials. *Opt. Express* **16**, 67–80 (2008).

33. N. Ji, D. E. Milkie, E. Betzig, Adaptive optics via pupil segmentation for high-resolution imaging in biological tissues. *Nat. Methods* **7**, 141–147 (2010).

34. J. Tang, R. N. Germain, M. Cui, Superpenetration optical microscopy by iterative multiphoton adaptive compensation technique. *Proc. Natl. Acad. Sci. U.S.A.* **109**, 8434–8439 (2012).

35. O. Katz, E. Small, Y. Guan, Y. Silberberg, Noninvasive nonlinear focusing and imaging through strongly scattering turbid layers. *Optica* **1**, 170–174 (2014).

36. I. N. Papadopoulos, J.-S. Jouhanneau, J. F. A. Poulet, B. Judkewitz, Scattering compensation by focus scanning holographic aberration probing (F-SHARP). *Nat. Photonics* **11**, 116–123 (2017).

37. E. H. Zhou, H. Ruan, C. Yang, B. Judkewitz, Focusing on moving targets through scattering samples. *Optica* **1**, 227–232 (2014).

38. C. Ma, X. Xu, Y. Liu, L. V. Wang, Time-reversed adapted-perturbation (TRAP) optical focusing onto dynamic objects inside scattering media. *Nat. Photonics* **8**, 931–936 (2014).

39. F. Kong, R. H. Silverman, L. Liu, P. V. Chitnis, K. K. Lee, Y. C. Chen, Photoacoustic-guided convergence of light through optically diffusive media. *Opt. Lett.* **36**, 2053–2055 (2011).

40. A. M. Caravaca-Aguirre, D. B. Conkey, J. D. Dove, H. Ju, T. W. Murray, R. Piestun, High contrast three-dimensional photoacoustic imaging through scattering media by localized optical fluence enhancement. *Opt. Express* **21**, 26671–26676 (2013).

41. T. Chaigne, O. Katz, A. C. Boccara, M. Fink, E. Bossy, S. Gigan, Controlling light in scattering media non-invasively using the photoacoustic transmission matrix. *Nat. Photonics* **8**, 58–64 (2014).

42. P. Lai, L. Wang, J. W. Tay, L. V. Wang, Photoacoustically guided wavefront shaping for enhanced optical focusing in scattering media. *Nat. Photonics* **9**, 126–132 (2015).

43. J. W. Tay, P. Lai, Y. Suzuki, L. V. Wang, Ultrasonically encoded wavefront shaping for focusing into random media. *Sci. Rep.* **4**, 3918 (2014).

44. X. Xu, H. Liu, L. V. Wang, Time-reversed ultrasonically encoded optical focusing into scattering media. *Nat. Photonics* **5**, 154–157 (2011).

45. Y. M. Wang, B. Judkewitz, C. A. DiMarzio, C. Yang, Deep-tissue focal fluorescence imaging with digitally time-reversed ultrasound-encoded light. *Nat. Commun.* **3**, 928 (2012).

46. K. Si, R. Fiolka, M. Cui, Fluorescence imaging beyond the ballistic regime by ultrasound-pulse-guided digital phase conjugation. *Nat. Photonics* **6**, 657–661 (2012).

47. H. Ruan, T. Haber, Y. Liu, J. Brake, J. Kim, J. M. Berlin, C. Yang, Focusing light inside scattering media with magnetic-particle-guided wavefront shaping. *Optica* **4**, 1337–1343 (2017).

48. H. Ruan, M. Jang, C. Yang, Optical focusing inside scattering media with time-reversed ultrasound microbubble encoded light. *Nat. Commun.* **6**, 8968 (2015).

49. B. F. Fosque, Y. Sun, H. Dana, C.-T. Yang, T. Ohyama, M. R. Tadross, R. Patel, M. Zlatic, D. S. Kim, M. B. Ahrens, V. Jayaraman, L. L. Looger, E. R. Schreiter, Labeling of active neural circuits in vivo with designed calcium integrators. *Science* **347**, 755–760 (2015).

50. H. H. Yang, F. St-Pierre, Genetically encoded voltage indicators: Opportunities and challenges. *J. Neurosci.* **36**, 9977–9989 (2016).

51. E. S. Boyden, F. Zhang, E. Bamberg, G. Nagel, K. Deisseroth, Millisecond-timescale, genetically targeted optical control of neural activity. *Nat. Neurosci.* **8**, 1263–1268 (2005).

52. D. G. Ouzounov, T. Wang, M. Wang, D. D. Feng, N. G. Horton, J. C. Cruz-Hernández, Y.-T. Cheng, J. Reimer, A. S. Tolias, N. Nishimura, C. Xu, In vivo three-photon imaging of activity of GCaMP6-labeled neurons deep in intact mouse brain. *Nat. Methods* **14**, 388–390 (2017).

53. J. P. Rickgauer, D. W. Tank, Two-photon excitation of channelrhodopsin-2 at saturation. *Proc. Natl. Acad. Sci. U.S.A.* **106**, 15025–15030 (2009).

54. B. K. Andrasfalvy, B. V. Zemelman, J. Tang, A. Vaziri, Two-photon single-cell optogenetic control of neuronal activity by sculpted light. *Proc. Natl. Acad. Sci. U.S.A.* **107**, 11981–11986 (2010).

55. E. Papagiakoumou, F. Anselmi, A. Bègue, V. de Sars, J. Glückstad, E. Y. Isacoff, V. Emiliani, Scanless two-photon excitation of channelrhodopsin-2. *Nat. Methods* **7**, 848–854 (2010).

56. R. Prakash, O. Yizhar, B. Grewe, C. Ramakrishnan, N. Wang, I. Goshen, A. M. Packer, D. S. Peterka, R. Yuste, M. J. Schnitzer, K. Deisseroth, Two-photon optogenetic toolbox for fast inhibition, excitation and bistable modulation. *Nat. Methods* **9**, 1171–1179 (2012).

57. A. M. Packer, D. S. Peterka, J. J. Hirtz, R. Prakash, K. Deisseroth, R. Yuste, Two-photon optogenetics of dendritic spines and neural circuits. *Nat. Methods* **9**, 1202–1205 (2012).

58. F. Zhang, V. Gradinaru, A. R. Adamantidis, R. Durand, R. D. Airan, L. de Lecea, K. Deisseroth, Optogenetic interrogation of neural circuits: Technology for probing mammalian brain structures. *Nat. Protoc.* **5**, 439–456 (2010).

59. I. Yamaguchi, T. Zhang, Phase-shifting digital holography. *Opt. Lett.* **22**, 1268–1270 (1997).

60. H. Ruan, M. Jang, B. Judkewitz, C. Yang, Iterative time-reversed ultrasonically encoded light focusing in backscattering mode. *Sci. Rep.* **4**, 7156 (2014).

61. K. Si, R. Fiolka, M. Cui, Breaking the spatial resolution barrier via iterative sound-light interaction in deep tissue microscopy. *Sci. Rep.* **2**, 748 (2012).

62. Y. Suzuki, J. W. Tay, Q. Yang, L. V. Wang, Continuous scanning of a time-reversed ultrasonically encoded optical focus by reflection-mode digital phase conjugation. *Opt. Lett.* **39**, 3441–3444 (2014).

63. C. Xiao, J. R. Cho, C. Zhou, J. B. Treweek, K. Chan, S. L. McKinney, B. Yang, V. Gradinaru, Cholinergic mesopontine signals govern locomotion and reward through dissociable midbrain pathways. *Neuron* **90**, 333–347 (2016).

64. J. Ryan Cho, J. B. Treweek, J. Elliott Robinson, C. Xiao, L. R. Bremner, A. Greenbaum, V. Gradinaru, Dorsal raphe dopamine neurons modulate arousal and promote wakefulness by salient stimuli. *Neuron* **94**, 1205–1219.e8 (2017).

65. C. K. Kim, S. J. Yang, N. Pichamoorthy, N. P. Young, I. Kauvar, J. H. Jennings, T. N. Lerner, A. Berndt, S. Y. Lee, C. Ramakrishnan, T. J. Davidson, M. Inoue, H. Bito, K. Deisseroth, Simultaneous fast measurement of circuit dynamics at multiple sites across the mammalian brain. *Nat. Methods* **13**, 325–328 (2016).

66. J. Y. Lin, P. M. Knutsen, A. Muller, D. Kleinfeld, R. Y. Tsien, ReaChR: A red-shifted variant of channelrhodopsin enables deep transcranial optogenetic excitation. *Nat. Neurosci.* **16**, 1499–1508 (2013).

67. M. Z. Lin, M. J. Schnitzer, Genetically encoded indicators of neuronal activity. *Nat. Neurosci.* **19**, 1142–1153 (2016).

68. M. Jang, C. Yang, I. M. Vellekoop, Optical phase conjugation with less than a photon per degree of freedom. *Phys. Rev. Lett.* **118**, 093902 (2017).

69. M. Jang, H. Ruan, B. Judkewitz, C. Yang, Model for estimating the penetration depth limit of the time-reversed ultrasonically encoded optical focusing technique. *Opt. Express* **22**, 5787–5807 (2014).

70. A. S. Chuong, M. L. Miri, V. Busskamp, G. A. C. Matthews, L. C. Acker, A. T. Sørensen, A. Young, N. C. Klapoetke, M. A. Henninger, S. B. Kodandaramaiah, M. Ogawa, S. B. Ramanlal, R. C. Bandler, B. D. Allen, C. R. Forest, B. Y. Chow, X. Han, Y. Lin, K. M. Tye, B. Roska, J. A. Cardin, E. S. Boyden, Noninvasive optical inhibition with a red-shifted microbial rhodopsin. *Nat. Neurosci.* **17**, 1123–1129 (2014).

71. A. A. Kaberniuk, A. A. Shemetov, V. V. Verkhusha, A bacterial phytochrome-based optogenetic system controllable with near-infrared light. *Nat. Methods* **13**, 591–597 (2016).

72. J. Brake, M. Jang, C. Yang, Analyzing the relationship between decorrelation time and tissue thickness in acute rat brain slices using multispeckle diffusing wave spectroscopy. *J. Opt. Soc. Am. A* **33**, 270–275 (2016).

73. A. Lev, B. Sfez, In vivo demonstration of the ultrasound-modulated light technique. *J. Opt. Soc. Am. A* **20**, 2347–2354 (2003).

74. M. M. Qureshi, J. Brake, H.-J. Jeon, H. Ruan, Y. Liu, A. M. Safi, T. J. Eom, C. Yang, E. Chung, In vivo study of optical speckle decorrelation time across depths in the mouse brain. *Biomed. Opt. Express* **8**, 4855–4864 (2017).

75. T. Laforest, A. Verdant, A. Dupret, S. Gigan, F. Ramaz, G. Tessier, Co-integration of a smart CMOS image sensor and a spatial light modulator for real-time optical phase modulation. *Proc. SPIE* **9022**, 90220N (2014).

76. M. Jang, H. Ruan, H. Zhou, B. Judkewitz, C. Yang, Method for auto-alignment of digital optical phase conjugation systems based on digital propagation. *Opt. Express* **22**, 14054–14071 (2014).

77. H. Ruan, M. L. Mather, S. P. Morgan, Pulsed ultrasound modulated optical tomography with harmonic lock-in holography detection. *J. Opt. Soc. Am. A* **30**, 1409–1416 (2013).

Citation: H. Ruan, J. Brake, J. E. Robinson, Y. Liu, M. Jang, C. Xiao, C. Zhou, V. Gradinaru, C. Yang, Deep tissue optical focusing and optogenetic modulation with time-reversed ultrasonically encoded light. *Sci. Adv.* **3**, eaao5520 (2017).